UCLA
UCLA Previously Published Works

Title
Rheology and Convective Heat Transfer of Colloidal Gas Aphrons in Horizontal Minichannels

Permalink
https://escholarship.org/uc/item/0rp7v6xp

Journal
International Journal of Heat and Fluid Flow, 27(2)

Authors
Tseng, H.
Pilon, L.
Warrier, G.

Publication Date
2006-01-02

Peer reviewed

eScholarship.org Powered by the California Digital Library
University of California

RHEOLOGY AND CONVECTIVE HEAT TRANSFER OF COLLOIDAL GAS APHRONS IN HORIZONTAL MINICHANNELS

Howard Tseng, Laurent Pilon*, and Gopinath R. Warrier

University of California, Los Angeles
Mechanical and Aerospace Engineering Department
420 Westwood Plaza, Los Angeles, CA 90095-1597

* Corresponding author:
Tel. +1 (310) 206-5598, Fax. +1 (310) 206-2302
E.mail:pilon@seas.ucla.edu

August 22, 2005

ABSTRACT

Colloidal gas aphrons (CGA) consists of closely packed minute gas bubbles with diameter ranging from 10 to 100 microns. It is produced by stirring a surfactant solution at high speed in a fully baffled beaker. CGA can be used in various applications such as bioremediation, bioreactors, oil recovery, and fire fighting. This paper reports experimental data for (1) adiabatic flow and (2) laminar convective heat transfer of CGA in five 1.58 x 0.76 mm^2 mini-rectangular channels. First, it is shown that CGA is a shear thinning fluid. Correlation for the friction factor as a function of Reynolds number is compared with that of water and *macro*foams. Then, the local temperature and heat transfer coefficient along the mini-channels are reported as a function of the mass flow rates and imposed heat flux. The heat transfer coefficients for CGA appears to be constant and independent of mass flow rate and imposed heat flux as well known for single phase laminar flow.

NOMENCLATURE

A_t	overall area of the channels, m^2
c_p	specific heat, J/kgK
D_h	hydraulic diameter based on the wetted perimeter, mm
f	Fanning friction factor
G	mass flux, kg/m^2s
h	local heat transfer coefficient, W/m^2K
$\bar{h}$	heat transfer coefficient in the thermally fully-developed region, W/m^2K
H	channel height, m
I	current, A
k	thermal conductivity, W/mK
L	total channel length, m
L_e	entry length, m
$\dot{m}$	total mass flow rate in the test section, kg/s
M	mass, kg
Nu	Nusselt number
$\overline{Nu}$	Nusselt number in the thermally fully-developed region, $= \bar{h}D_h / k_{H_2O}$
P	channel perimeter, m
Pr	Prandtl number
ΔP	overall pressure drop, Pa
Q_f	volumetric flow rate per channel, m^3/s
$q_{channels}$	total heat input in the five channels, W
q_{loss}	heat losses, W
q_{total}	total heat transfer rate ($= VI = q_{channels} + q_{loss}$), W
q_w''	wall heat flux, W/m^2
Re	Reynolds number
T	temperature, K
t	time, s
u_f	average fluid velocity in a channel, m/s

U	power supply voltage, V
V	volume, m^3
W	channel width, m
x	axial coordinate, m
x^+	dimensionless axial length, $x^+ = 2x / D_h \, Re \, Pr$

Symbols

$\dot{\gamma}_w$	effective shear rate, 1/s
$\dot{\gamma}_a$	apparent shear rate, 1/s
μ_e	effective dynamic viscosity, mPa.s
ρ_f	fluid density, kg/m^3
τ_w	wall shear stress, Pa
ε	specific expansion ratio, ρ_L / ρ_{CGA}
ϕ	volume fraction of air in CGA or porosity, V_{air} / V_{CGA}
ψ	mass fraction of air in CGA, M_{air} / M_{CGA}

Subscripts

air	refers to air in CGA
CGA	refers to CGA
f	working fluid
H_2O	refers to single phase water
in	refers to inlet
out	refers to outlet
x	refers to local value at location x
w	refers to the wall

1. INTRODUCTION

1.1 Motivations

Colloidal Gas Aphrons (CGA), also called microfoams, consist of bubbles between 10 and 100 μm in diameter with a porosity of up to 70%. They can be produced by stirring an aqueous surfactant solution contained in a fully baffled beaker at room temperature, as described in Figure 1 [1]. The solution is stirred by a spinning disk driven at 5,000 to 10,000 rpm by an electrical motor. Two to four baffles are equally spaced around the container and extend well above the surface of the solution. Once a critical stirring speed has been reached, waves are produced at the liquid surface. The waves beat up against the baffles and are forced to re-enter the liquid at the baffles. It is believed that the re-entering liquid carries a thin film of gas which becomes sandwiched between the liquid and the baffle. Such a thin film is unstable and breaks into microscopic bubbles encapsulated by a soapy shell, i.e. minute gas aphrons. After a few minutes of stirring, CGA forms and rises at the surface of the solution. It has been reported that CGAs made of water and surfactant solutions (i) have stable bubbles with a narrow and reproducible size distribution (see Figure 2), (ii) exhibit high stability, (iii) separate easily from the bulk liquid phase, and (iv) can be easily pumped through tubes while keeping their structure [1]. However, even though the flow properties of CGA have been discussed qualitatively in the literature, to the best of our knowledge, no quantitative data on the rheology, pressure drop, and friction factor associated with CGA flow in pipes has been reported.

Colloidal gas aphrons are subject to the same physical phenomena as those taking place in foams including (i) liquid drainage, (ii) interbubble gas diffusion, and (iii) Gibbs-

Marangoni effects [2]. However, capillary drainage or Plateau border suction effect occurring in polyhedral foams [2] does not take place in CGA as bubbles are spherical (see Figure 2). Moreover, buoyancy caused by the density difference between the gas and the liquid phases is relatively limited due to the small size of the microbubbles that act as colloidal particles.

Most applications of colloidal gas aphrons take advantage of (i) their large interfacial area, (ii) the adsorption of particles at the microbubble interfaces, and (iii) their stability for enhanced mass transfer [3]. Possible applications include (1) separation, (2) oil recovery, (3) firefighting, (4) fermentation and bioreactors, (5) material synthesis, and wherever macroscopic foams are currently being used.

Application of CGAs to separation technology include (i) remediation of soils contaminated with hydrocarbons [4,5], (ii) cleaning of water contaminated with metals [6-8] or organic dyes [9,10], (iii) protein separation [11-15] in replacement of a combination of processes including centrifugation, filtration, extraction and chromatography, (iv) cell flotation [16] such as yeast-cells [17], (iv) mineral extraction by flotation [18], (v) algae removal from contaminated waters [1].

Colloidal gas aphrons have been used for cleaning sand contaminated with oil [5] and could be used for oil recovery when foams are currently being used (see for example Refs.[19-21] and references therein). Experiments shows that CGA formed with anionic surfactants percolate through sand carrying most of the oil [1]. Note that CGA formed with cationic surfactant will not percolate through the sand bed [1].

Foam is currently used for fire fighting by covering the burning material with a thick layer of foam. However, it is difficult to pump large flow rates of foams through often

long pipes and various fittings [22]. Moreover, pipe fitting are responsible for pressure drop much larger in foam flows than in single phase water flows [22]. Colloidal gas aphrons were reported "to flow like water" [1] and therefore could be used for fire fighting as they would travel longer distances than foam for identical pumping power or pressure drop. Thus, they could increase mobility, reactivity, and safety of fire-fighters. Sebba [1] indicated that CGA made of a surfactant mixture can very effectively extinguish gasoline fire. A mixture of anionic and cationic surfactant was shown to spread over the burning gasoline and extinguish the fire.

Applications of CGA to fermentation take advantage of their large interfacial area and their long lifetime and slow rise. Indeed, fermentation reactors based on bubble columns or bioreactors are often mass transfer limited due to (1) relatively small interfacial area and (2) rapid rise and thus short residence time of the large bubbles through the reactor. The use of CGA was instrumental in increasing oxygen transfer from the bubble to the solution and resulted in faster growth of oxygen consuming micro-organisms [1]. In a recent study, Dai *et al*. [23] showed that oxygen transfer increases with temperature but depends on stirring speed as well as the type and concentration of the surfactant. Depending on the surfactant used, mass transfer may actually decrease most likely due to the mass transfer resistance caused by the surfactant shell (see Figure 2a). Also, the mass transfer increases with stirring speed but remains constant beyond 8,000rpm.

Tin powder with controlled particle size has been synthesized using the CGA production setup described in Figure 1 [24]. More recently, Davey *et al*. [25] used CGA process to synthesize closed-cell microfoams consisting of interconnected glycine crystal network having 90% porosity and bubble diameter ranging from 10 to 30μm.

In most of these applications, CGA is pumped through columns, pipes, and fitting under different thermal conditions. For these reasons, it is necessary to understand the rheology and the heat transfer properties of CGA.

1.2 CGA Structure

There are still many unresolved questions regarding the formation and the structure of Colloidal Gas Aphrons and current explanation remain speculative [26]. The most widely accepted structure was first suggested by Sebba [1]. It speculates that bubbles have a multilayered shell as shown in Figure 2a but no direct observation or physical models have demonstrated such a structure. The main supporting arguments were (i) the absence of bubble coalescence, (ii) the fact that hydrophobic globules attach to the surface of the bubbles, and (iii) that when the CGA is created in dyed water and the generated bubbles are transferred into clear water, the bubbles contained some dyed water in their shell. Finally, Sebba [1] did not elaborate on the thickness of the soapy shell. Amiri and Woodburn [27] estimated the thickness of the soapy shell to be 750 nm for cationic surfactant CTAB. They studied the liquid drainage rate in CGA dispersion and the bubble rise velocity. Bredwell and Worden [3] estimated the shell thickness to be 200-300 nm for nonionic surfactant Tween-20, based on the study of gas diffusion from the CGA bubble to the liquid bulk, assuming that the mass transfer is limited by the rate of diffusion across the shell. More recently, Jauregi *et al*. [26] employed freeze fracture with TEM and X-ray diffraction to study the structure of the soapy shell. They imaged and measured the thickness of the "surfactant" shell to be 96 nm. They argued that the shell does not provide room for finite inner water phase as proposed by Sebba [1] and shown in Figure 2a. Thanks to X-ray diffraction study, they showed that the soapy shell

consisted of more than one layer of surfactant molecules. However, they noticed a large uncertainty on the exact number of layers.

2. EXPERIMENTAL SETUP

Figure 3 shows a schematic of the cross-section of the test section. The design is similar to that used by Warrier *et al*. [28] to study boiling heat transfer in mini-channels. Five identical rectangular parallel mini-channels have been machine etched into Lexan® polycarbonate top. They are mated with an aluminum bottom plate. An Inconel-625 heating strip is placed beneath the aluminum plate and has the same dimensions of 6.35 mm wide and 30.72 cm long. An additional Teflon® strip of identical dimension is placed between the aluminum plate and the heating element to assure good thermal contact and provide electrical insulation. A Sorensen DC S8-125E power supply with voltage ranging from 0 to 60 volts and current ranging from 0 to 125A is used for resistance heating of the Inconel-625 strip. Each flow channel has a hydraulic diameter D_h of 1.03 mm defined based on the wetted perimeter. The total length to diameter ratio L/D_h is 315.6 while the effective heated length to diameter ratio is 298.4. The distance between the centers of any two adjacent channels is 3.0 mm. The apparatus rests on a G10 board. Two Omega PX26-015DV pressure transducers are used to measure the overall pressure drop between the inlet and the outlet of the channels. Thanks to the short length of the test section we can safely assume that the pressure gradient is constant along the channels, i.e., $dP/dx \approx -\Delta P/L$ [29]. Moreover, recent experimental studies on foams have confirmed this assumption [30].

The inlet and outlet temperatures are measured by type K thermocouples. Moreover, to measure the surface temperature along the aluminum plate, ten indentations were made

in the aluminum plate. Holes were machined into the Teflon® and Inconel-625 strips to allow the thermocouples to pass through. They allow ten type-K thermocouples to be secured on the aluminum by high thermal conductivity thermocouple cement. There are two thermocouples per axial location and the temperature readings at each axial location did not differ by more than ±0.2°C for all heat transfer experiments. The five axial location measured from the entrance are 0.029m, 0.080m, 0.154m, 0.227m, and 0.278m. The average of both temperatures is taken as the temperature of the heated surface at that axial location. The large thermal conductivity of the aluminum plate allows for uniform heat flux along the channels. Also, the temperature of the aluminum plate at a given cross-section perpendicular to the flow is assumed to be uniform by virtue of the fact that the Biot number ($Bi = hL/k_{Al}$) is much smaller than unity. Thus, the surface temperature in the channel is identical to that measured at the aluminum plate/heating strip interface. Also, heat losses through the Lexan® top are neglected due to its low thermal conductivity (0.2 W/mK). They were conservatively estimated to be 100 mW or less than 0.3% of the total heat input.

As mentioned by Warrier *et al*. [28], it was not possible to measure the fluid flow temperature inside the channels because the thermocouples were in contact with the channel walls leading to a higher temperature reading. Instead, the local fluid temperature is computed using the local energy balance equation. To minimize contact resistance between the Inconel-625 heating strip and the aluminum bottom plate, several clamps are used to ensure good thermal contact between the heating strip and the aluminum plate. All the thermocouples and pressure readings are recorded every second by an IOTECH DAQTEMP 14A data acquisition system connected to a computer.

2.1 Experimental Procedure

Figure 4 shows the water experimental setup, which consists of (i) a fifteen gallon Nalgene supply tank, (ii) a Cole-Parmer model 75225 volumetric pump, (iii) a Cole-Parmer P-32464-46 single float flowmeter (rotameter type), (iv) the test section, (v) Sorensen DC S8-125E power supply, and (vi) the return tank. The same methodology as described by Warrier *et al*. [28] is followed for the single phase water experiments. First, the liquid is preheated in the supply tank. After reaching the desired temperature, it is pumped through the flowmeter into the test section where a heat flux may be applied by imposing a current and voltage across the heating strip. Each experiment is allowed to run for a minimum of 10 minutes so that steady-state conditions are reached. Then, the data acquisition unit is turned on to record the pressures and temperatures. The typical overall duration of a single experiment is about 20 to 25 minutes. When the experiment is completed, the current and voltage are changed for the same flow rate. The process is repeated for different flow rates.

For adiabatic tests, the power to the heating element is turned off and the temperature along the length of the channels is constant. Water then flows out of the test section and into the return tank, where it is cooled off by chilled water running through copper tubes. When the water has reached 23°C, it is then drained back into the supply tank. This process is repeated for each water experiment.

The volumetric flow rate of single phase water is measured directly with the Cole-Parmer flowmeter. The flowmeter is first calibrated by pumping single phase water into a graduated cylinder. A stop watch is used to measure the time it takes to fill a certain volume. The error in the flowmeter reading is estimated to be ±5% at 25°C. The mass flow rates for the water experiments are calculated by multiplying the density of water at

the inlet temperature [31] by the volumetric flow rate. The error associated with the water mass flow rates is the same as the error of the graduated cylinder used for the calibration of the flowmeter.

The experimental setup used in the CGA experiments is similar to that used with water except that the supply tank is replaced by a fully baffled container as shown in Figure 1. The flowmeter is also removed as it strongly affects the CGA morphology. Instead, the mass and volumetric flow rates are determined by measuring the mass $M_{CGA}(t)$ and the volume $V_{CGA}(t)$ of the CGA flowing in and out of the test section as a function of time using the same procedure as that used for calibrating the flowmeter for the single phase flow. The mass of CGA was measured at different times using a scale with an error reading of ±1 gram. The mass flow rate was computed by curve fitting the plot of mass versus time over a period of time larger than 300s. It varied from 0.9 to 9 g/s.

Moreover, since the mass of air is significantly smaller than that of water, we assume that $M_{total}(t) \approx M_{water}(t)$. Then, the porosity of CGA can be expressed as,

$$\phi(t) = \frac{V_{gas}(t)}{V_{CGA}(t)} = 1 - \frac{M_{CGA}(t)}{\rho_{water} V_{CGA}(t)} \tag{1}$$

Figure 5 shows the mass of CGA flowing out of the test section versus time under adiabatic conditions while Figure 6 plots the volume of CGA versus time for different heat input but identical pump setting. Both mass and volume of CGA increase linearly with time with a regression coefficient larger than 0.99. The slopes of the linear curve fitting correspond to the mass and volumetric flow rates. The volumetric flow rate is larger for heated flows. Moreover, the porosity decreases from up to 71% to as low as

64% as the volumetric flow rate increases from 0.9 cm^3/s to 5 cm^3/s while it increases slightly (by about 4%) as the heat input increases from 0 to 130 W.

Finally, Figure 7 shows micrographs of CGA samples taken at the inlet and outlet of the test section observed under a Leica DM IL microscope. In all cases, it was verified that no appreciable change can be observed in both the porosity and the bubble size distribution as CGA travels through the mini-channels. Figure 8 shows the size distribution of CGA bubbles measured from 536 bubbles using the image analysis software Image J. One can see that the majority of the bubbles are smaller than 100 microns. Finally, in the case of convective heat transfer experiments the porosity and bubble diameter tend to increase slightly due to gas expansion but are within the experimental uncertainty of 3%.

According to the specifications of the Omega PX26-015DV pressure transducers, there is a 1% error reading on the pressure reading corresponding to an absolute error of 1,000 Pa. Note that the tubing connecting the pressure transducers to the inlet and outlet fixtures was filled with the working fluid prior to each run to reduce the error readings on the pressure.

The thermocouples have been calibrated by flowing water through the test section under adiabatic conditions at temperature ranging from 25 to 50^{o}C. The mean difference between all the thermocouples and the fluid temperature (measured at the inlet and outlet of the test section) was ±0.2°C. Steps were also taken to minimize the influence of the heating element on the thermocouple wire by enlarging thermocouple passages in the Inconel-625 strip. Table 1 shows the list of experimentally measured variables and the associated experimental uncertainty.

3. RHEOLOGY OF COLLOIDAL GAS APHRONS

There exists a large body of literature studying the rheological properties of liquid foams. It is beyond the scope of the present study to present a thorough review. Instead, the reader is referred to Refs. [32-37] and references therein for detailed discussion.

3.1 Effective Viscosity

The CGA is treated as a pseudo-homogeneous time-independent non-Newtonian fluid obeying power-law behavior in steady-state laminar flow and having effective viscosity μ_e. The wall shear stress τ_w, the wall shear rate $\dot{\gamma}_w$, and the apparent shear rate $\dot{\gamma}_a$ are related by,

$$\tau_w = k\dot{\gamma}_w^n = \mu_e\dot{\gamma}_a \tag{2}$$

where k and n are the flow consistency and flow behavior, respectively. If n equals unity then (i) the fluid is Newtonian, (ii) $\dot{\gamma}_w$ and $\dot{\gamma}_a$ are identical, and (iii) k is the dynamic viscosity. On the contrary, the wall shear rate is defined in terms of the apparent shear rate by the Rabinowitsch-Mooney relationship expressed as,

$$\dot{\gamma}_w = \left(\frac{3n+1}{4n}\right)\dot{\gamma}_a \tag{3}$$

The wall shear stress τ_w and the apparent shear rate $\dot{\gamma}_a$ are experimentally determined from the pressure drop ΔP and the average fluid velocity u_f as [38],

$$\tau_w = \frac{D_h \Delta P}{4L} \qquad \text{and} \qquad \dot{\gamma}_a = \frac{8u_f}{D_h} \tag{4}$$

The average fluid velocity u_f in a single channel is calculated by dividing the volumetric flow rate for each channel Q_f by the overall cross sectional area of the channel, i.e., $u_f = Q_f/(WH)$. The hydraulic diameter D_h of the rectangular ducts is defined based on the

wetted perimeter. Note that the apparent shear rate simplifies to $\dot{\gamma}_a = 32Q_f / \pi D_h^3$ for cylindrical pipes. Figure 9 shows the shear stress and the viscosity of single phase water and CGA as a function of the apparent shear rate under adiabatic conditions at 25°C. First, the validity of the experimental procedure and data analysis procedures is demonstrated by the single phase water data. Indeed, water data indicates that the shear stress is linearly proportional to the shear rate, i.e., water is a Newtonian fluid with a viscosity of 0.866 mPa.s at 25°C. This value falls within 2% of the tabulated value of 0.88 mPa.s [31]. Similar results were obtained at 35°C.

On the other hand, CGA behaves as a shear thinning fluid for which the effective viscosity decreases with apparent shear rate. The shear stress and apparent shear rate correlate as follows,

$$\tau_w = 0.122\dot{\gamma}_a^{0.56} \tag{5}$$

corresponding to an effective viscosity of $\mu_e = 122\dot{\gamma}_a^{-0.44}$ for shear rates varying between 1,000 and 7,000s^{-1}. The above correlations for the shear stress and effective viscosity of CGA as a function of shear rate have regression coefficients of 0.92 and 0.88, respectively.

The CGA shear stress versus the shear rate plot in Figure 9 shows significant scattering due to changes of the CGA porosity with flow rates and heat input. Moreover, the above analysis is valid for incompressible fluids. However, CGA is a compressible non-Newtonian fluid which can be analyzed using the volume equalization method proposed by Economides and co-workers [38,39] and successfully applied to flow of macrofoams. The volume equalized power law relates the volume equalized stress to the volume equalized shear rate as,

$$\frac{\tau_w}{\varepsilon} = K_{VE}\left(\frac{\dot{\gamma}_a}{\varepsilon}\right)^n \tag{6}$$

where K_{VE} and n are empirical constant while ε is the specific expansion ratio defined as ρ_L/ρ_{CGA}. The density of CGA, ρ_{CGA}, is experimentally determined by dividing the mass flowrate by the volumetric flowrate. Figure 10 shows the volume equalized shear stress versus the shear rate. Similarly to macroflow of foams [38,39], the CGA data collapses to a single curve with $K_{VE} = 0.062$, n = 0.588, and a regression coefficient of 0.95.

3.2 Fanning Friction Factor vs. Reynolds Number

The Fanning friction factor is defined as [31],

$$f = \frac{\tau_w}{\rho_f u_f^2/2} \tag{7}$$

where τ_w is the wall shear stress [Equation (5)], ρ_f is the fluid density, and u_f is the average fluid velocity in a single channel. The Fanning friction factor for single phase water in laminar flow in a rectangular channel of cross section (1.58x0.76 mm^2) is given by [31],

$$f_{l\phi} = \frac{15.5}{Re} \tag{8}$$

where *Re* is the Reynolds number, defined as,

$$Re = \frac{GD_h}{\mu} \tag{9}$$

where *G* is the mass flux and μ is the fluid dynamic viscosity. Similarly, the friction factor for foam flowing in cylindrical pipe has been reported as [40],

$$f_{foam} = \frac{15.97}{Re^{0.99}} \tag{10}$$

where the Reynolds number is computed from the effective foam viscosity [22]. To the best of our knowledge, no friction factor has been reported for CGA flow. However, it is essential in designing and scaling up bench-top experiments to industrial processes and in predicting pressure drop and pumping requirement.

The friction factor for CGA can also be calculated using Equations (4) and (7). The Reynolds number for CGA is defined based on the effective viscosity μe of the CGA given by $\mu_e = 122\dot{\gamma}_a^{-0.44}$. Figure 11 compares the values of the friction factor versus Reynolds number obtained experimentally for CGA under adiabatic and heat flow conditions with reported correlations for single phase water and foams. One can see that the adiabatic water experimental data coincides with the water correlation given by Equation (8). Using a power-law curve fit for the data, the derived friction factor for CGA is 16.21/Re and the regression error is 0.99.

4. CONVECTIVE HEAT TRANSFER

Single and two-phase (liquid/vapor) convective heat transfer in mini- and microchannels have been the subject of intense studies [41,42]. Here again, it is beyond the scope of this work to present a thorough review of the topic. Instead, we first validate our experimental apparatus and procedure with single-phase water. Then, we report experimental data for the local temperatures and local and fully-developed heat transfer coefficients for convective heat transfer to CGA under imposed heat flux.

4.1 Heat Loss

To determine the heat loss of the power supply to the surrounding environment, an energy balance is performed on the heated water. The total power input is expressed by Joule's law,

$$q_{total} = UI \tag{11}$$

where U is the voltage measured in volts and I is the current measured in ampere. The actual heat input into the test section $q_{channels}$ must account for the heat loss to the surrounding and is given by,

$$q_{channels} = q_{total} - q_{loss} \tag{12}$$

It can also be calculated from the energy balance on the single phase water,

$$q_{channels} = \dot{m}_{H_2O} c_{p,H_2O} (T_{H_2O,out} - T_{H_2O,in}) \tag{13}$$

where $\dot{m}_{H_2O}$ is the mass flow rate and c_{p,H_2O} is the specific heat of water at the average temperature. Figure 12 plots the values of $q_{channels}$ computed from Equation (13) versus q_{total} measured using Equation (11). It was found that the heat loss to the environment q_{loss} varies linearly with the total power input q_{total} and represents at most 8% of the total heat input over the range from 42 to 130 W. In other words, at least 92% of the total power consumed is supplied to the test section.

4.2 Specific Heat of CGA

The specific heat, $C_{p,CGA}$, for CGA is not known but can be determined using the energy balance equation

$$c_{p,CGA} = \frac{q_{channels}}{\dot{m}_{CGA} (T_{CGA,out} - T_{CGA,in})} \tag{14}$$

Since the experimental test section and procedure remain the same for both CGA and water, it is assumed that the $q_{channels}$ for CGA represents also 92% of q_{total}. Then, the experimental data indicate that the specific heat of CGA is 3,954 J/kgK at the average temperature $(T_{f,out} + T_{f,in})/2$ of 30°C compared to 4,178 J/kgK in the case of single

phase water. Using mass and energy balance equations, the specific heat of CGA can be modeled as,

$$c_{p,CGA} = (1-\psi)c_{p,H_2O} + \psi c_{p,air} \tag{15}$$

where ψ is the mass fraction of air in CGA, i.e.,

$$\psi = \rho_{air}\phi/[\rho_{air}\phi + \rho_{H_2O}(1-\phi)] \tag{16}$$

Experimentally, the mass fraction x and the porosity ϕ are such that $x = 2.6\text{x}10^{-3}$ and ϕ = 69%. Then, Equation (15) predicts the specific heat of CGA to be 4,170 J/kgK which falls within 6% of the experimental value.

4.3 Local Temperature Profile

As previously mentioned, the local fluid temperature along the channels is not measured. Instead, it is estimated using the energy balance equation,

$$T_f(x) = T_{f,in} + \frac{q_{channels}}{\dot{m}_f c_{p,f}} x = T_{f,in} + \left(\frac{T_{f,out} - T_{f,in}}{L}\right)x \tag{17}$$

where $T_{f,in}$ and $T_{f,out}$ are the measured fluid inlet and outlet temperatures, $\dot{m}_f$ is the total mass flow rate of the working fluid, and x is the axial location of the thermocouples along the aluminum plate measured from the channel entrance (x = 0). The uncertainty in the calculated liquid temperatures is estimated to be 10%.

Figures 13a and b show the typical wall and fluid temperature profiles along the channel for water and CGA, respectively. In both cases, the volumetric flow rate is 2.9×10^{-6} m^3/s, the total heat input in the channels is 130 W, and the inlet temperature is 25°C. The difference between the fluid and the wall surface temperature increases in the entry region and remains constant in the thermally fully-developed region for both water and

CGA. However, the temperature difference is much larger for CGA due to smaller specific heat and heat transfer coefficient as discussed later.

4.4 Nusselt Number and Heat Transfer Coefficient

The wall heat flux q''_w is calculated from the overall heat input $q_{channels}$ in the five channels and is given by,

$$q''_w = \frac{q_{channels}}{A_t} \tag{18}$$

where A_t is the total heated surface area of the five channels. For the five channels heated uniformly on three sides, $A_t = 5(W+2H)L$ where W, H and L are the width, height, and length of a single channel. Then, the local heat transfer coefficient can be calculated according to

$$h(x) = \frac{q''_w}{T_w(x) - T_f(x)} \tag{19}$$

where $T_w(x)$ is the measured wall temperature at the location of the thermocouple and $T_f(x)$ is the fluid temperature calculated using Equation (17). A finite difference simulation for two-dimensional steady-state heat conduction in the aluminum plate with uniform heat flux on one side and spatially dependent heat transfer coefficient on the other was developed. The results show that axial heat conduction along the length of the channel is negligible for the test conditions of this study except very close to the two ends. The large thermal conductivity of the aluminum plates allows one to neglect thermal resistance and to assume that the temperature reading gives the wall temperature within experimental uncertainty. In addition, the Biot number in the transverse direction is small in all cases (less than 0.02) and the temperature is assumed constant at each cross-section of the aluminum plate.

For the sake of validation, the single phase water data are presented in terms of the local Nusselt number defined as $Nu_{x,H_2O} = h_{H_2O}(x)D_h / k_{H_2O}$ where D_h is the wetted hydraulic diameter of the channel and k_{H_2O} is the fluid thermal conductivity. Numerical simulations reported by Wibulswas [43] and reproduced in the literature [44] were used for comparison as they are the available results the most analogous to our experimental boundary conditions. Indeed, the simulations [43] corresponds to thermally developing flow of single-phase in rectangular channels with aspect ratios of 2.00 and 3.00 with constant heat flux at the bottom and constant surface temperature peripherally while neglecting axial heat conduction. In the present study, the aspect ratio of the channels under consideration is 2.08 and falls between the two simulated geometries while the rectangular duct was heated on three sides and had one adiabatic wall. Figure 14 shows the evolution of the local Nusselt number along the dimensionless axial length x^+ for single phase water and heat transfer rate $q_{channels}$ ranging from 8,857 to 27,621 W/m^2. The dimensionless axial length x^+ is defined as $2x / D_h \, Re \, Pr$ where x is the dimensional axial location and Pr is the Prandtl number. In calculating the Prandtl and Reynolds numbers, the fluid properties are determined using the average of the inlet and outlet temperatures. The Prandtl number ranges from 5.452 to 5.988 while the Reynolds number ranges from 506 to 1223.

Furthermore, fully-developed steady-state flow occurs when $x^+ = 0.1$ [43]. One can see that the local Nusselt number decreases in the entry region as the thermal boundary develops to reach a constant value nearly independent of heat flux in the thermally fully-developed region. Moreover, the experimental data falls between the simulated values, except at the entry region. This can be attributed to (1) axial heat conduction, (2)

measurement uncertainty on $\Delta T = T_w(x) - T_f(x)$, and (3) the difference in boundary conditions (e.g., parabolic velocity profile at the entrance, constant sidewall temperature) between the numerical simulations and the experimental conditions. Overall, these results confirm the accuracy of the instrumentation and the validity of the data analysis. Therefore, the same analysis can be confidently applied to CGA.

In the case of CGA, the local heat transfer coefficient $h_{CGA}(x)$ can be determined using Equation (19). However, the traditional Nusselt number cannot be calculated since the thermal conductivity of CGA is unknown unless one relies on possibly inaccurate models. Instead, the Nusselt number for CGA is defined as $Nu_{x,CGA} = h_{CGA}(x) D_h / k_{H_2O}$ where D_h is the hydraulic diameter of the channel and k_{H_2O} is the water thermal conductivity at the average fluid temperature. Figure 15 compares the local Nusselt number versus the dimensionless axial length x^+ for CGA and water. The thermal conductivity as well as the Reynolds, and Prandtl numbers for water have been used for calculating x^+ values for both water and CGA. In laminar heat convection with uniform wall heat flux for both single phase water and CGA, the local Nusselt number and heat transfer coefficient appear to be nearly independent of the heat input and of the mass flow rate in the thermally fully-developed region. However, for CGA the thermally fully-developed region appears later ($x^+ > 0.1$) than for water. Moreover, the convective heat transfer rate achieved with CGA is much less than water for the same heat flux and mass flow rate. For single phase flow of water, the uncertainty in the calculated local heat transfer coefficient varies from 23.1% to 3.6% as the power input increases from 42 W to 130 W. Similarly, for CGA, assuming $C_{p,CGA}$ = 3,954 J/kgK, the uncertainty in the local

heat transfer coefficient decreases from 15.1% to 2.2% as the power input varies from 42 to 130 W.

Figure 16 shows the plot of the heat transfer coefficient versus the mass flow rate in the thermally fully-developed region. It indicates that the heat transfer coefficient for both water and CGA is independent of mass flux. The heat transfer coefficient for single-phase water under fully developed laminar flow conditions in rectangular ducts with three walls subject to constant heat flux and the fourth side adiabatic, is about 2,546 W/m^{2}K corresponding to $\overline{Nu} = \bar{h}D_h / k_{H_2O} = 6.3$. On the other hand, numerical simulations giving the Nusselt number for single-phase fully developed laminar flow in rectangular ducts have been reported in the literature [44]. However, we were unable to find simulations matching all the experimental boundary conditions of this study. The closest studies include that of Shah and London [44] who reported the Nusselt number of 3.02 in a rectangular duct of aspect ratio H/W=0.5 with four uniformly heated walls. It corresponds to a heat transfer coefficient for water of 1800 W/m^{2}K. Schmidt and Newell [45] graphically reported a Nusselt number of 3.15 (defined based on the wetted perimeter [44]) in rectangular ducts with aspect ratio 2.08 and one wall uniformly heated wall, one adiabatic wall, and two walls with uniform temperature corresponding to a heat transfer coefficient of 1,878 W/m^{2}K. The large differences (around 40%) between the numerical simulations and the present experimental data can be attributed (i) the differences in the boundary conditions between the simulations and the experimental data, (ii) the fact that the fully-developed regime may not have been reached, (iii) the Lexan top wall is very rough thus disturbing the boundary layers and the heat transfer.

Moreover, the heat transfer coefficient for thermally fully-developed CGA flows also remains constant for different volumetric flow rates and heat fluxes. However, it is reduced by 39% compared to that obtained with water and equal to 1,548 W/m^2K. This can be attributed to the large porosity of CGA resulting in significant reduction in the effective thermal conductivity and specific heat. The effective thermal conductivity of two-phase media can be estimated by various models. Most models fall between the Maxwell's model and the series model [46]. For CGA, the Maxwell-Garnett model gives the upper bound with $k_{eff}=k_{water}[2k_{water}+k_{air}-2\phi(k_{water}-k_{air})]/[2k_{water}+k_{air}+\phi(k_{water}-k_{air})]$, while the series model give the lower bound with $k_{eff} = (1-\phi)k_{water}+ \phi k_{air}$. Using these two limiting models, the Nusselt number for CGA is estimated to range between 8 (series model) and 12 (Maxwell-Garnett's model). In both cases, the Nusselt number is larger for CGA than for single phase with identical thermal conductivity under laminar flow and imposed heat flux. This could be attributed to possible slip velocity of CGA at the wall. Then, the shear thinning model and the effective viscosity used to compute the Reynolds number will no longer be valid. Note also that for thermally fully-developed laminar convective heat transfer of plug flow under imposed heat flux, the Nusselt number for fully developed flow is equal to 8 [47].

Finally, note that for both water and CGA, the measured heat transfer coefficients for water and CGA lead to Biot numbers for the aluminum plate smaller than 0.02 thus confirming our initial approximation that the plate temperature is uniform at any cross-section perpendicular to the flow.

5. CONCLUSIONS

The present study was concerned with rheology and heat transfer properties of colloidal gas aphrons flowing in rectangular mini-channels with hydraulic diameter of 1.03 mm. First, well-known properties and correlations for single phase water were used to validate the experimental apparatus and data analysis. Experimental studies were performed for colloidal gas aphrons and the following conclusions can be drawn:

1. CGA behaves as a shear thinning fluid whose effective viscosity varies with the apparent shear rate according to $\mu_e = 122\dot{\gamma}_a^{-0.44}$ for the present geometry for shear rates varying from 1,000 to 7,000 s^{-1}.
2. The friction factor for CGA in laminar flow follows the same law as single phase, i.e., f=15.5/Re with the Reynolds number computed from the effective viscosity of CGA.
3. The local heat transfer coefficients and Nusselt numbers for CGA under imposed heat flux and laminar flow conditions are independent of the mass flow rate and heat flux.
4. The heat transfer coefficient for CGA made of water and surfactants is smaller than for single phase water due to its high porosity resulting in reduced specific heat and thermal conductivity.

Future work should attempt to visualize the CGA bubbles in the channels in order to assess their interaction with each other and with the heated walls.

ACKNOWLEDGMENTS

The authors are indebted to Dean. Vijay K. Dhir for useful technical discussions and for facilitating access to key pieces of equipment.

REFERENCES

[1] Sebba, F., 1987. *Foams and Biliquid Foams-Aphrons*, John Wiley & Sons, New York.

[2] Bhakta, A., and Ruckenstein, E., 1997. *Decay of standing foams: drainage, coalescence and collapse*, Advances in Colloid and Interface Science, (**70**), pp. 1-124.

[3] Bredwell, M.D., and Worden, R.M., 1998. *Mass transfer properties of microbubbles: 1) Experimental studies*, Biotechnology Progress, (**14**), pp. 31-38.

[4] Kommalapati, R.R., Valsaraj, K.T., Constant, W.D. and Roy, D., 1998. *Soil flushing using colloidal gas aphron suspensions generated from a plant-based surfactant*, Journal of Hazardous Materials, (**60**), pp. 73-78.

[5] Roy, D., Valsaraj, K.T., Constant, W.D., and Darji, M., 1994. *Removal of hazardous oily waste from a soil matrix using surfactants and colloidal gas aphron suspensions under different flow conditions*, Journal of Hazardous Materials, (**38**), pp. 127-144.

[6] Roy, D., Kommalapati, R.R., Valsaraj, K. T., and Constant, W. D., 1995. *Soil flushing of residual transmission fluid: Application of Colloidal Gas Aphron suspensions and conventional surfactant solutions*, Water Research, (**29**), pp. 589-595.

[7] Ciriello, S., Barnett, S.M., and Deluise, F.J., 1982. *Removal of heavy-metals from aqueous-solutions using microgas dispersions*, Separation Science and Technology, (**4**), pp. 521-534.

[8] Cabezon, L.M., Caballero, M., Diaz, J.M., and Perezbustamante, J.A., 1991. *Multi-elemental separation and determination of some heavy-metals (Cu, Co, Cd, and Ni) in tap water and high salinity media by CGA (Colloidal Gas Aphron) coflotation*, Analysis, (**4**), pp. 123-127.

[9] Roy, D., Valsaraj, K.T. and Kottaisa, S.A., 1992. *Separation of organic-dyes from waste-water by using colloidal gas aphrons*, Separation Science and Technology, (**27**), pp. 573-588.

[10] Basu, S., and Malpani, P.R., 2001. *Removal of methyl orange and methylene blue dye from water using colloidal gas aphron-effect of processes parameters*, Separation Science and Technology, (**13**), pp. 2997-3013.

[11] Noble, M., Jauregi, P., Kaul, A., and Varley, J., 1998. *Protein recovery using gas-liquid dispersions*, Journal of Chromatography, (**1-2**), pp. 31-43

[12] Jauregi, P., Varley, J., and Gilmour, S., 1997. *Characterization of gas aphrons for subsequent use for protein recovery*, Chemical Engineering Journal, (**65**), pp. 1-11.

[13] Jauregi, P., and Varley, J., 1998. *Colloidal gas aphrons: A novel approach to protein recovery*, Biotechnology and Bioengineering, (**59**), pp. 471-481.

[14] Amiri M.C., and K. T. Valsaraj, 2004. *Effect of gas transfer on separation of whey protein with aphron flotation*, Separation and Purification Technology, (**35**), pp. 161-167.

[15] Jarudilokkul, S., Rungphetcharat, K., and Boonamnuayvitaya, V., 2004. *Protein separation by colloidal gas aphrons using nonionic surfactant,* Separation and Purification Technology, (**35**), pp. 23-29.

[16] Subramaniam, M.B., Blakebrough, N., and Hashim, M.A., 1990. *Clarification of suspensions by colloidal gas aphrons*, Journal of Chemical Technology and Biotechnology, (**48**), pp. 41-60.

[17] Hashim, M.A., Sengupta, B., and Subramaniam M.B., 1995. *Investigations of the flotation of yeast-cells by colloidal gas aphrons (CGA) dispersions*, Bioseparation, (**5**), pp. 167-173.

[18] Cilliers, J. J., and Bradshaw, D. J., 1996. *The flotation of fine pyrite using colloidal gas aphrons*, Minerals Engineering, (**9**), pp. 235-241.

[19] Schramm, L. L., 1994. *Foams : fundamentals and applications in the petroleum industry,* American Chemical Society, Washington, DC.

[20] Kovscek, A.R., and Radke, C.J., 1994. *Fundamentals of Foam Transport in Porous Media*, in FOAMS Fundamentals and Applications in the Petroleum Industry, Advances in Chemistry Series 242, ed. Laurier L. Schramm, Chapter 3, pp. 113-163 1994.

[21] Joseph, D.D., Kamp, A.M., and Bai, R., 2002. *Modeling foamy oil in porous media*, International Journal of Multiphase Flow (**28**), pp.1659-1686.

[22] Deshpande, N.S., and Barigou, M., 2001. *The flow of gas-liquid foams through pipe fittings*, International Journal of Heat and Fluid Flow, (**22**), pp. 94-101.

[23] Dai, Y., Deng, T., Wang, J., and Xu, K., 2003. *Enhancement of oxygen gas–liquid mass transfer with colloidal gas aphron dispersions*, Colloids and Surfaces A: Physicochemical and Engineering Aspects, Vol. 240, pp.165-171.

[24] Riviello A.E., Young D., Sebba F., 1994. *A novel method for production of finely divided tin metal powders*, Powder Technology, **(78)**, pp. 19-24.

[25] Davey, R.J., Alison, H., Cilliers, J.J., and Garside, J., 1998. *A new strategy for preparing macroporous materials: using a colloidal gas aphron to create an oriented crystal network*, Chemical Communications, (**23**), pp. 2581-2582.

[26] Jauregi, P., Mitchell, G.R., Varley, J., 2000. *Colloidal gas aphrons (CGA): Dispersion and structural features*, American Institute of Chemical Engineering Journal, **(46)**, pp. 24-36.

[27] Amiri, M.C., Woodburn, E.T, 1990. *A method for the characterization of colloidal gas aphron dispersions*, Chemical Engineering Research and Design, **(68)**, pp. 154-160.

[28] Warrier, G.R., Dhir, V.K. and Momda, L.A., 2002. *Heat transfer and pressure drop in narrow rectangular channels*, Experimental Thermal and Fluid Sciences, (**26**), pp. 53-64.

[29] Gardiner, B.S., Dlugogorski, B.Z., and Jameson, G.J., 1998. *Rheology of fire-fighting foams*, Fire Safety Journal, **(31)**, pp.61-75.

[30] Briceño, M.I., and Joseph, D.D., 2003. Self-lubricated transport of aqueous foams in horizontal conduits, International Journal of Multiphase Flow, **(29)**, pp. 1817-1831.

[31] Munson, B.R., Young, D.F., and Okiishi, T.H., 1994. *Fundamental of Fluid Mechanics*, John Wiley & Sons, New York.

[32] Bikerman, J. J., 1973. *Foams*. Applied physics and engineering Series, Vol. 10 Springer-Verlag, New York, NY.

[33] Kraynick, A.M., 1987. *Foam flows*, Annual Reviews in Fluid Mechanics, (**20**), pp.325-327.

[34] Kraynick, A.M., and Hansen, M.G., 1987. *Foam rheology: A model of viscous phenomena*, Journal of Rheology, (**31**), pp.175-205.

[35] Calvert, J.R., and Nezhati, K., 1985. *A rheological model for a liquid-gas foam*, International Journal of Heat and Fluid Flow, (**7**) pp. 164-168.

[36] Princen, H.M., 1983. *Rheology of foams and highly concentrated emulsions, I. Elastic properties and yield stress of a cylindrical model system*, Journal of Colloidal and Interface Science (**91**), pp.160-175.

[37] Prud'homme, R. K., and Khan, S. A., 1996. *Experimental results on foam rheology. Foams : theory, measurements, and applications*, edited by R. K. Prud'homme, S. A. Khan. Surfactant science series, vol. 57, Marcel Dekker, New York.

[38] Enzendorfer, C., Harris, R.A., Valko, P., Econmides, M.J., Fokker, P.A., and Davies, D.D., 1995. *Pipe viscometry of foams*, Journal of Rheology, **(39)**, pp. 345-356.

[39] Valko, P. and Econmides, M.J., 1992. *Volume equalized constitutive equations for foamed polymer solutions*, Journal of Rheology, **(36)**, pp. 111-127.

[40] Gracia, F., Gracia, R., Padrino, J.C., Mata, C., Trallero, J.L., and Joseph, D.D., 2003. *Power law and composite power law friction factor correlations for laminar and turbulent gas-liquid flow in horizontal pipelines*, International Journal of Multiphase Flow, (**29**), pp. 1605-1624.

[41] Qu, W., and Mudawar, I., 2002. *Experimental and numerical study of pressure drop and heat transfer in a single phase micro-channel heat sink*, International Journal of Heat and Mass Transfer, (**45**), pp. 2549-2565.

[42] Morini, G.L., 2004. *Single-phase convective heat transfer in microchannels: a review of experimental results*, International Journal of Thermal Sciences, (**43**), pp. 631-651.

[43] Wibulswas, P., 1966. *Ph.D thesis*, London University.

[44] Shah, R.K and London, A.L., 1978. *Laminar Flow Forced Convection in Ducts: A Source Book for Compact Heat Exchanger Analytical Data*, Academic Press, New York.

[45] Schmidt, F. W. and Newell, M. E., 1967. *Heat transfer in fully developed laminar flow through rectangular and isosceles triangular ducts*, Vol. 10, pp. 1121-1123.

[47] Belova, I.V., and Murch, G.E., 2004. *Monte Carlo simulation of the effective thermal conductivity in two-phase material,* Journal of Materials Processing Technology, (**153-154**), pp. 741-745.

[48] Rohsenow, W. M. and Choi H. Y. 1961. *Heat, mass, and momentum transfer*, Prentice-Hall, Englewood Cliffs, N.J.

LIST OF FIGURES AND TABLE CAPTIONS

Measured Quantity	Measured Uncertainty
Volume, V	± 5 mL
Mass, M	± 1.0 gram
Pressure, P	1% (1000 Pa)
Volumetric flow rate, Q_f	± 5%
Temperature, T	± 0.2°C
Voltage, U	± 0.01 V
Current, I	± 0.01 A

Table 1: Uncertainty associated to each experimental measurement.

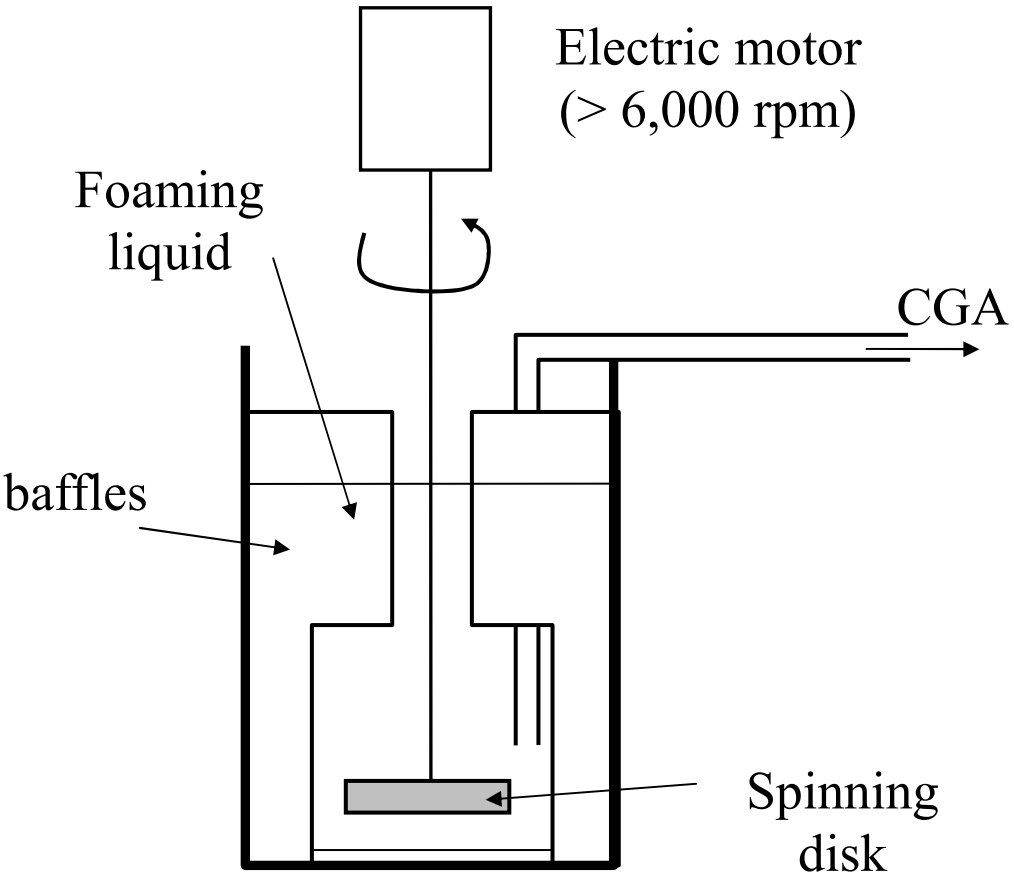

Figure 1. Schematic of the CGA forming process.

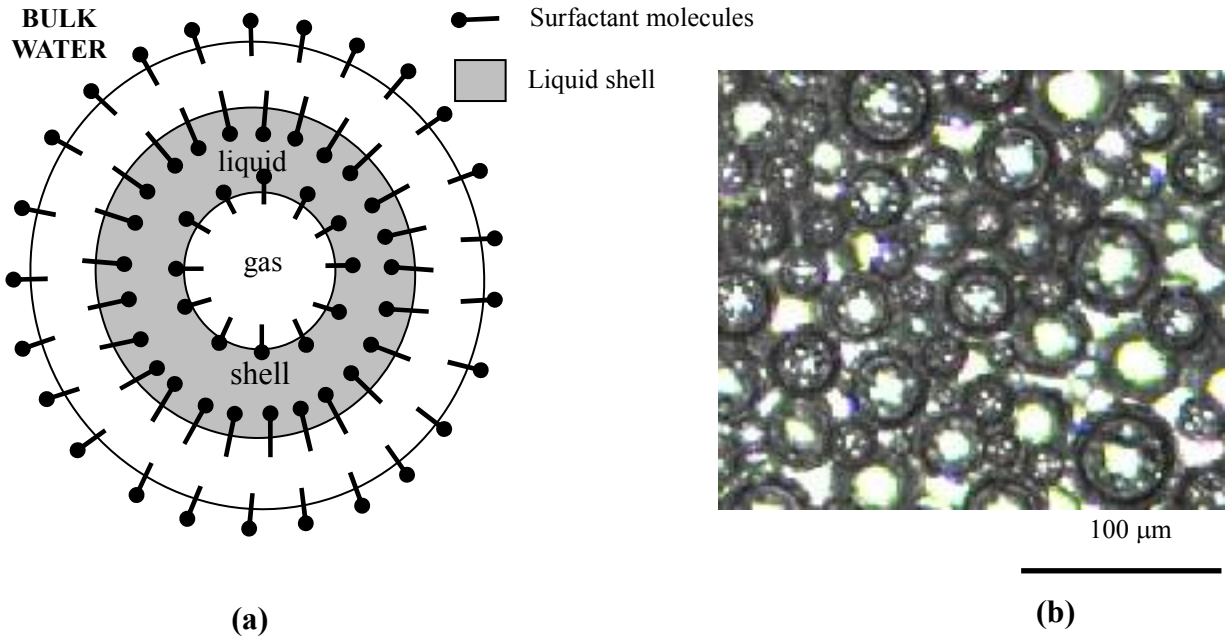

Figure 2. Microbubble with encapsulated surfactant film in aqueous Colloidal Gas Aphrons (a) schematic based on structure proposed by Sebba [1] (b) micrograph of actual CGA.

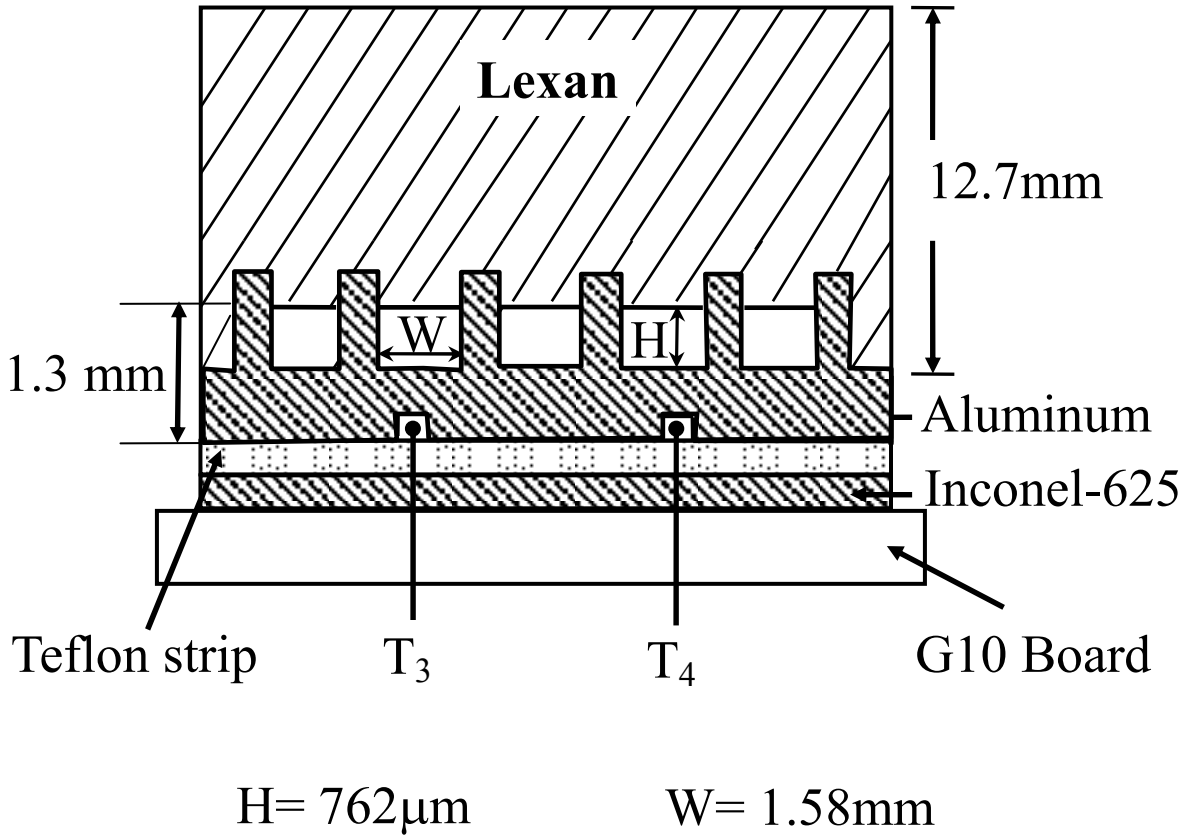

Figure 3. Cross-section of the minichannels.

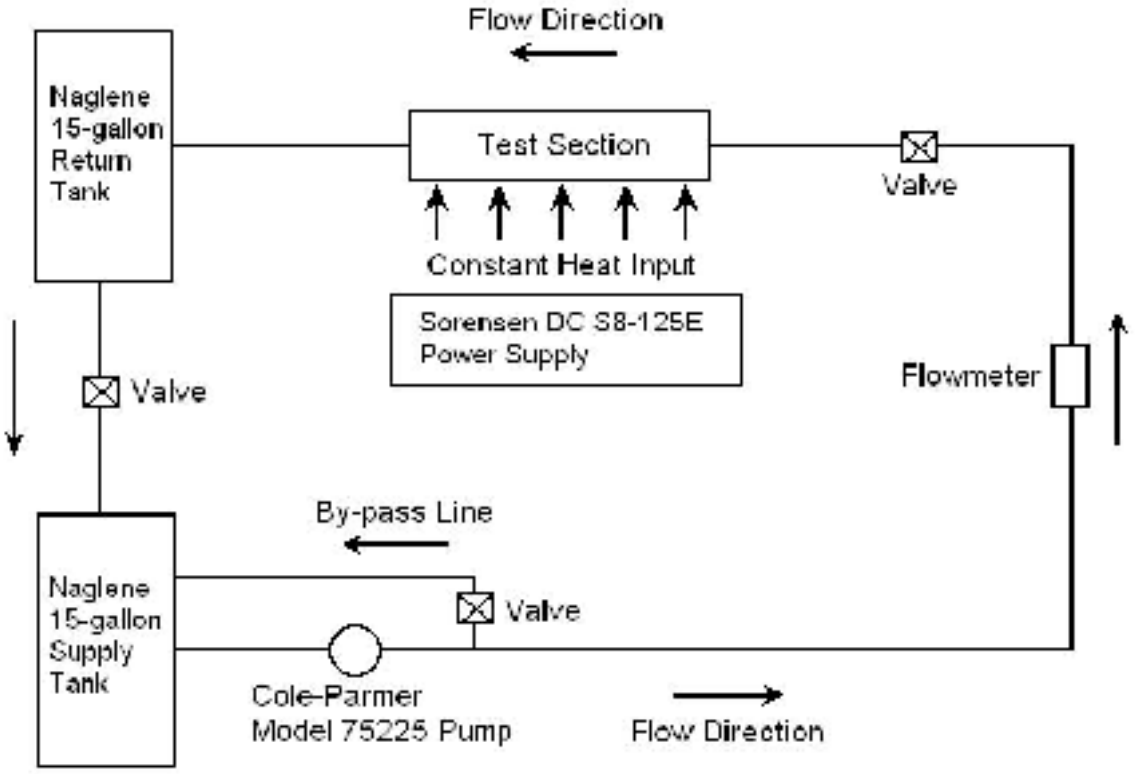

Figure 4. Water flow loop.

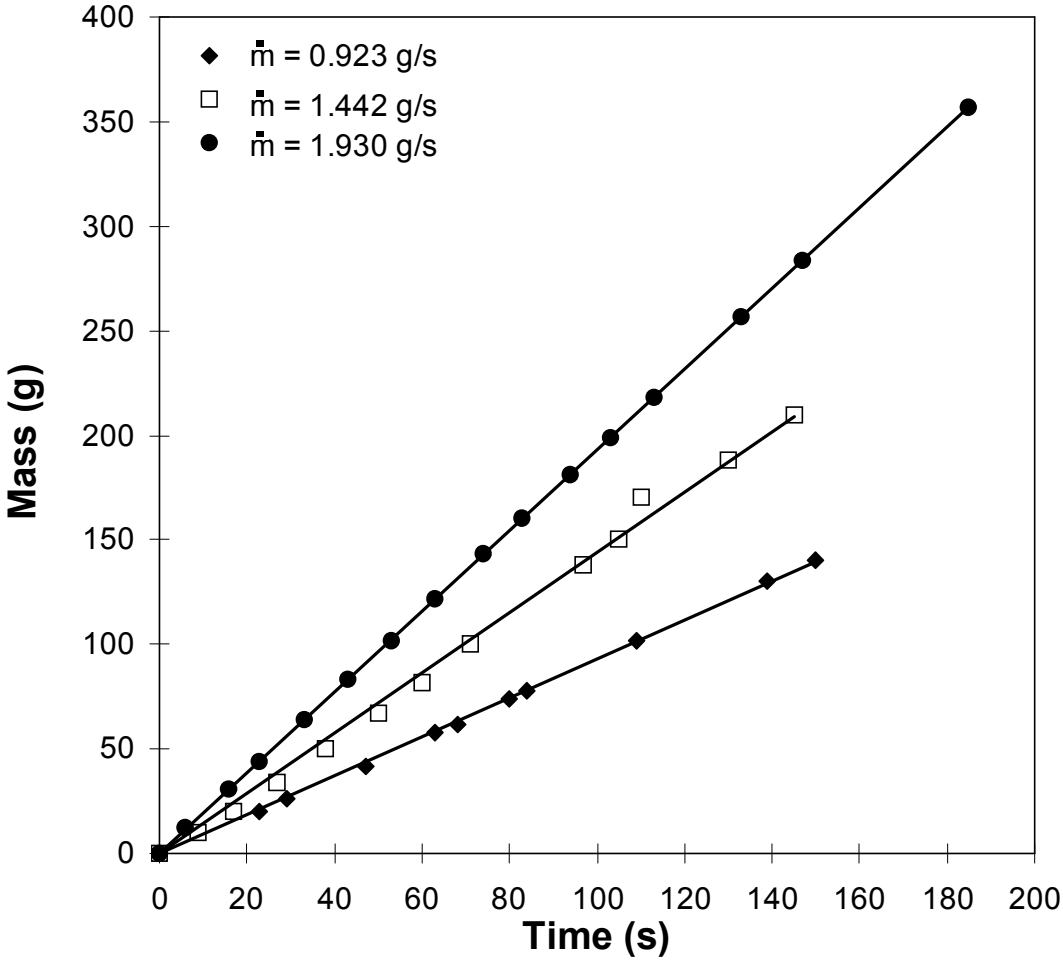

Figure 5. Mass of out flowing CGA versus time for adiabatic flow at 25°C.

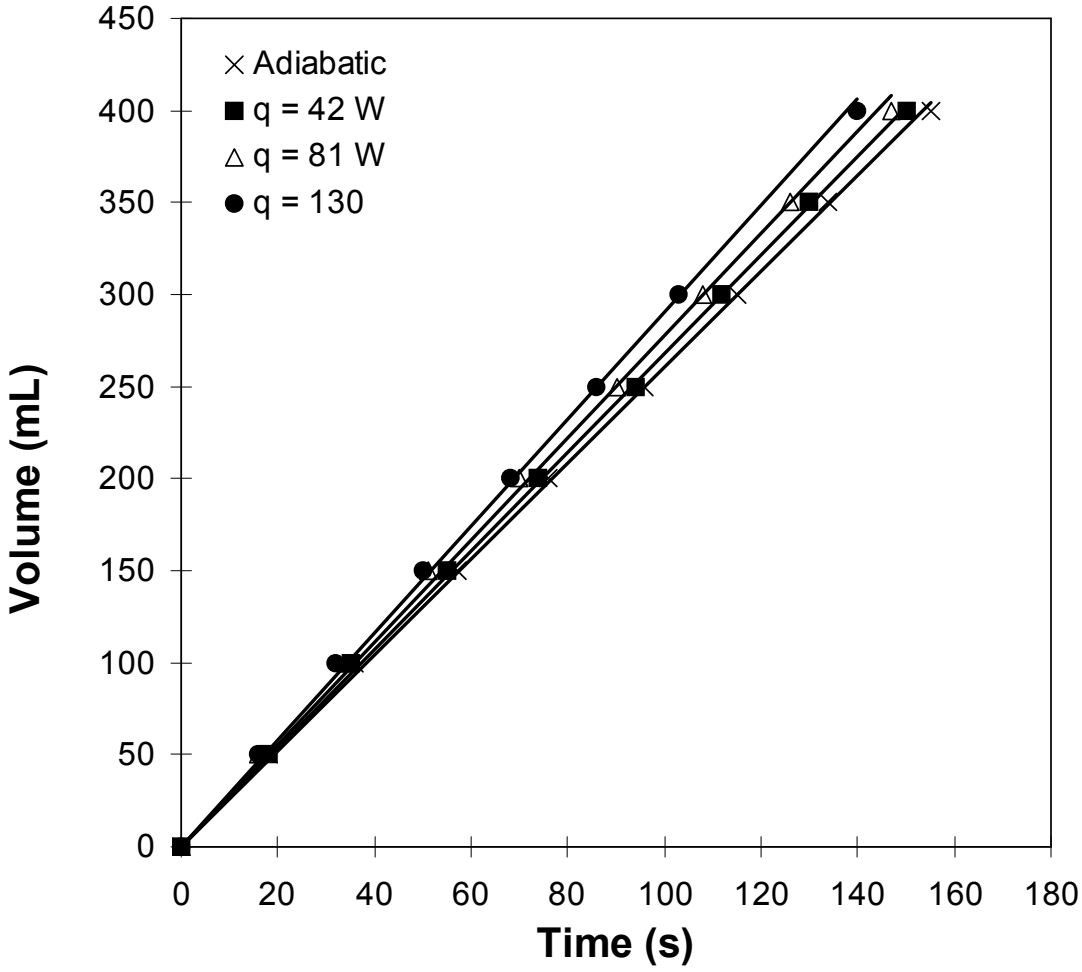

Figure 6. Volume of out flowing CGA versus time for different heat input but identical pump setting.

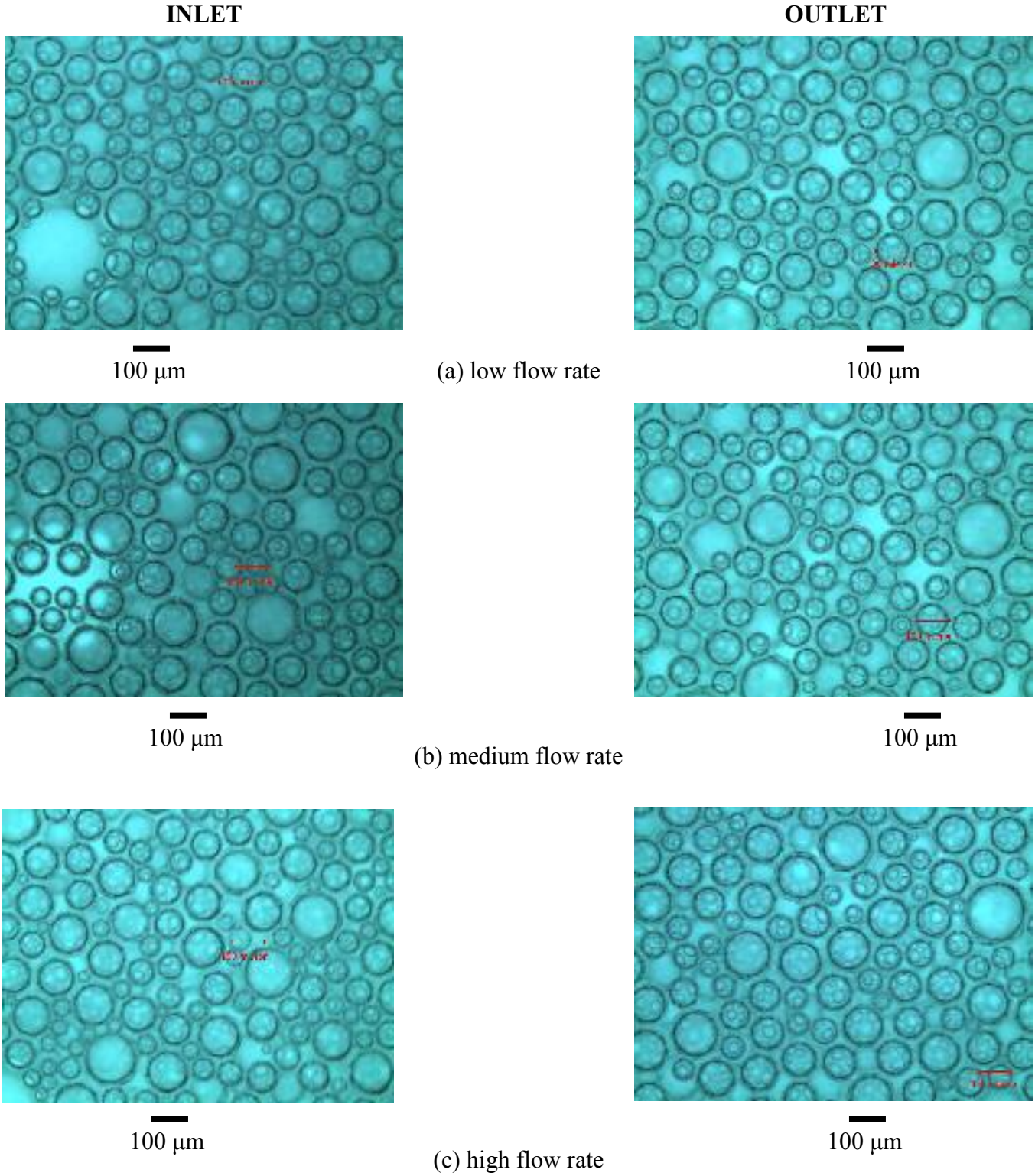

Figure 7. CGA bubble size before and after flowing into the channels for (a) 4.91×10^{-4} kg/s, (b) 8.25×10^{-4} kg/s, and (c) 12.8×10^{-4} kg/s.

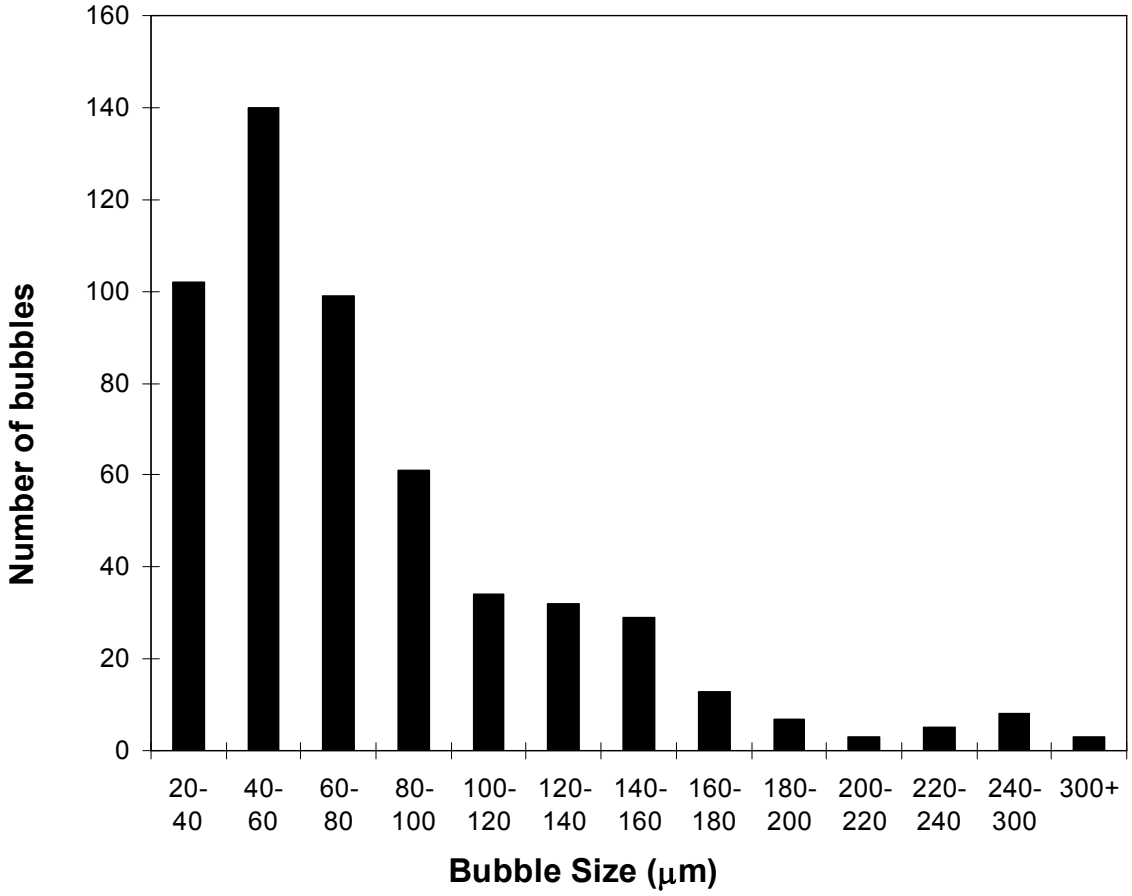

Figure 8. Bubble size distribution for bubbles flowing in rectangular channels.

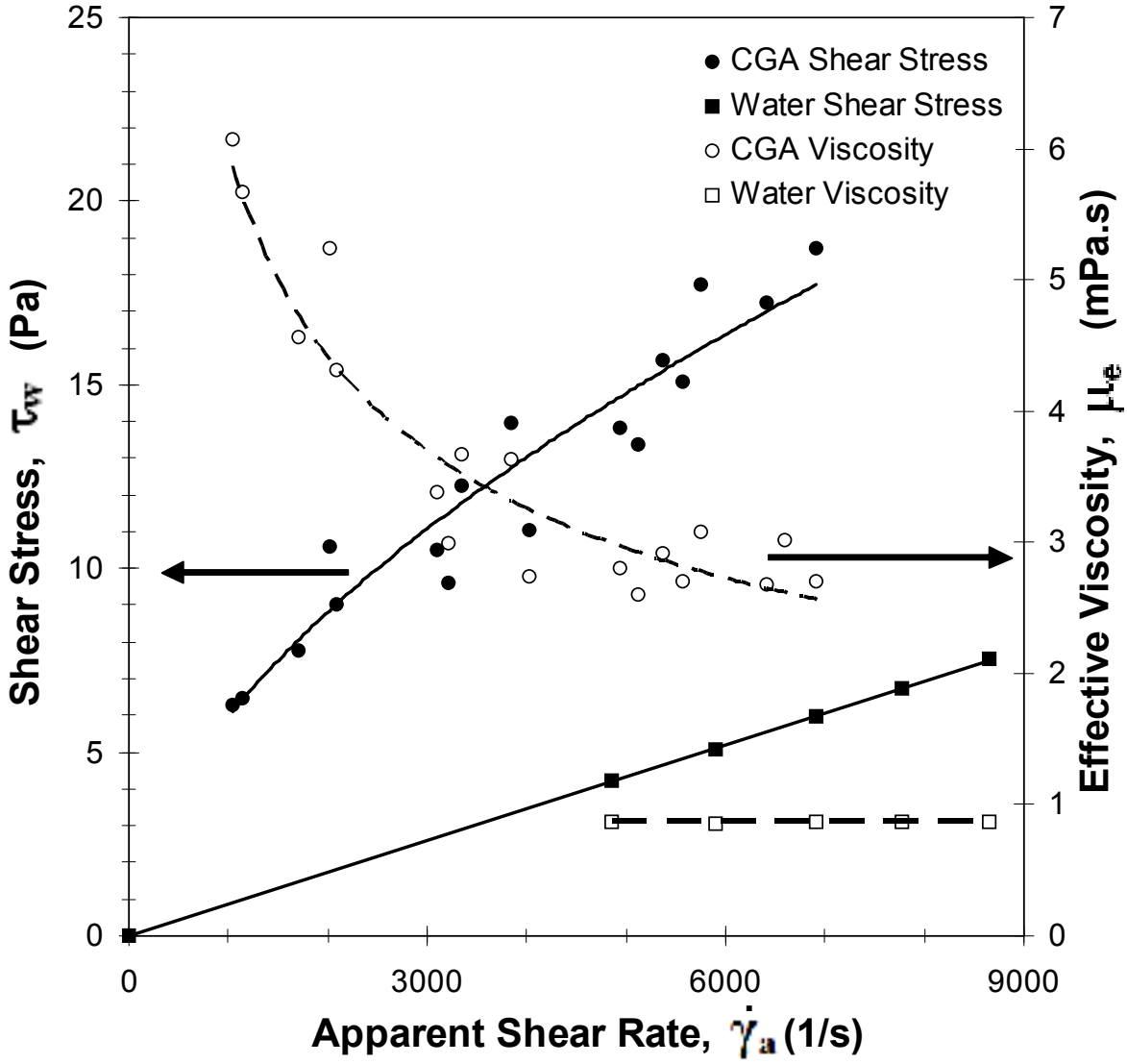

Figure 9. Shear stress and effective viscosity versus apparent shear rate for both adiabatic water and CGA at 25°C.

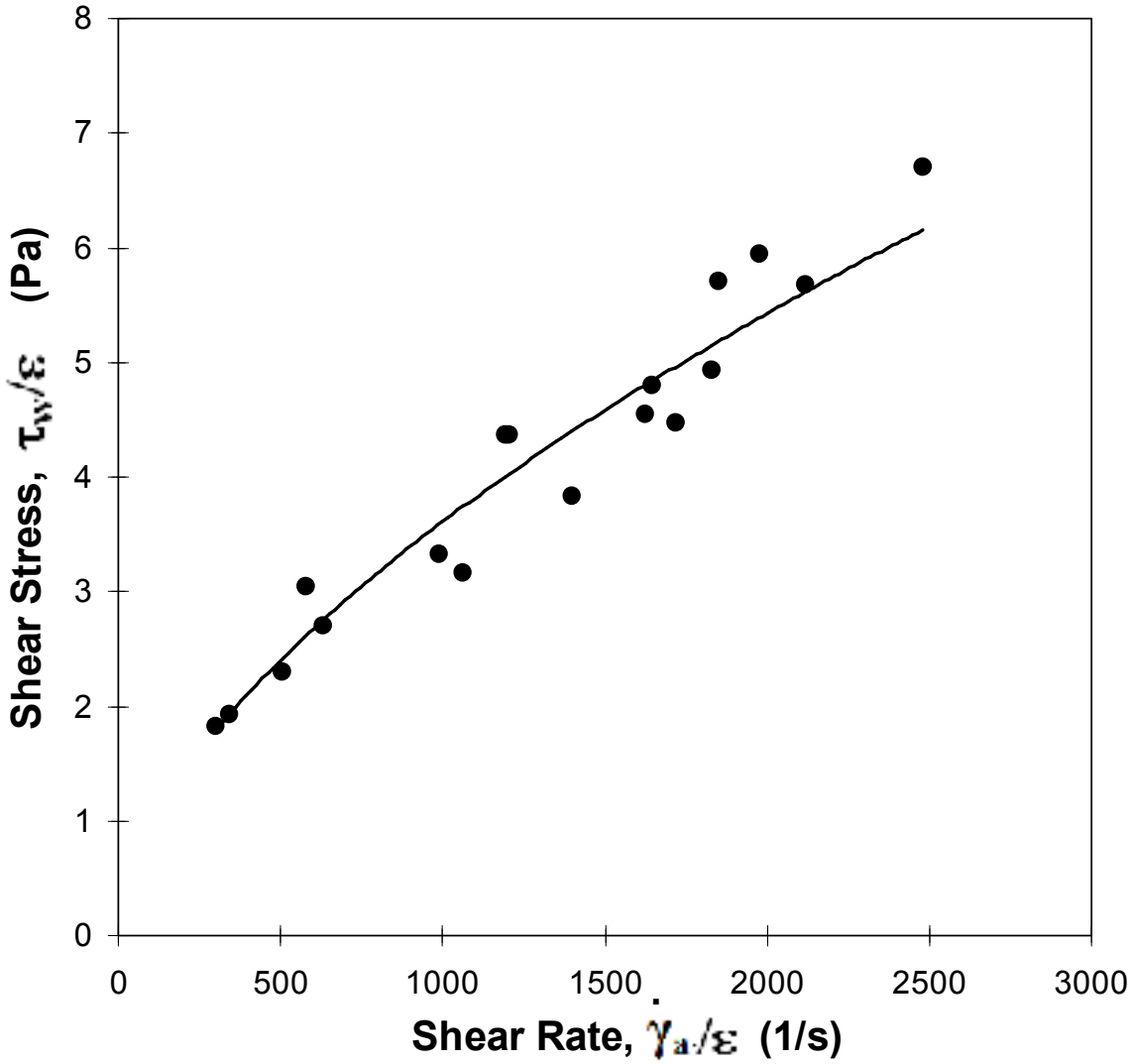

Figure 10. Volume equalized shear stress versus volume equalized apparent shear rate for adiabatic CGA at 25°C.

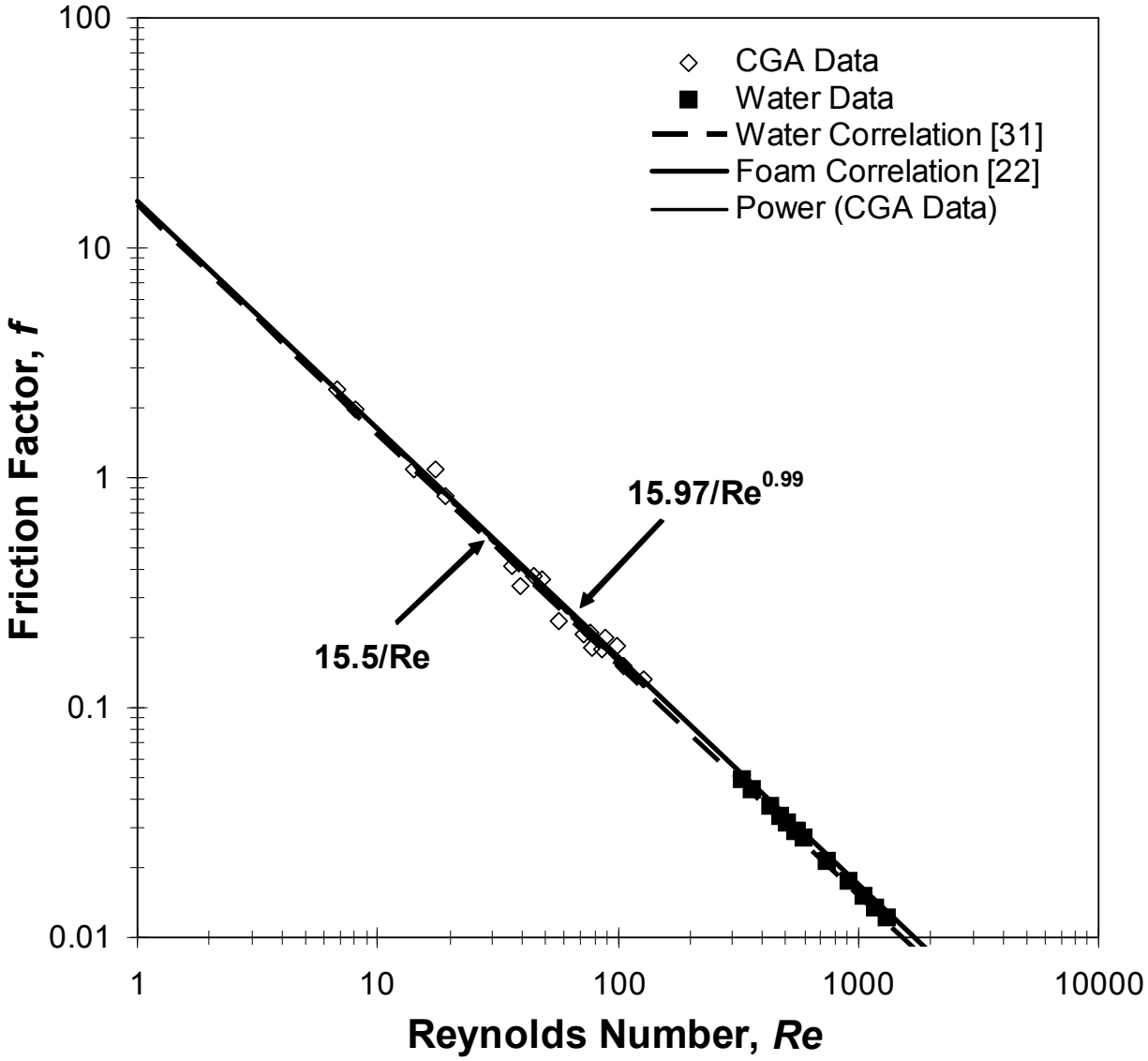

Figure 11. Friction factor versus Reynolds number for both adiabatic and heated experimental data for water and CGA.

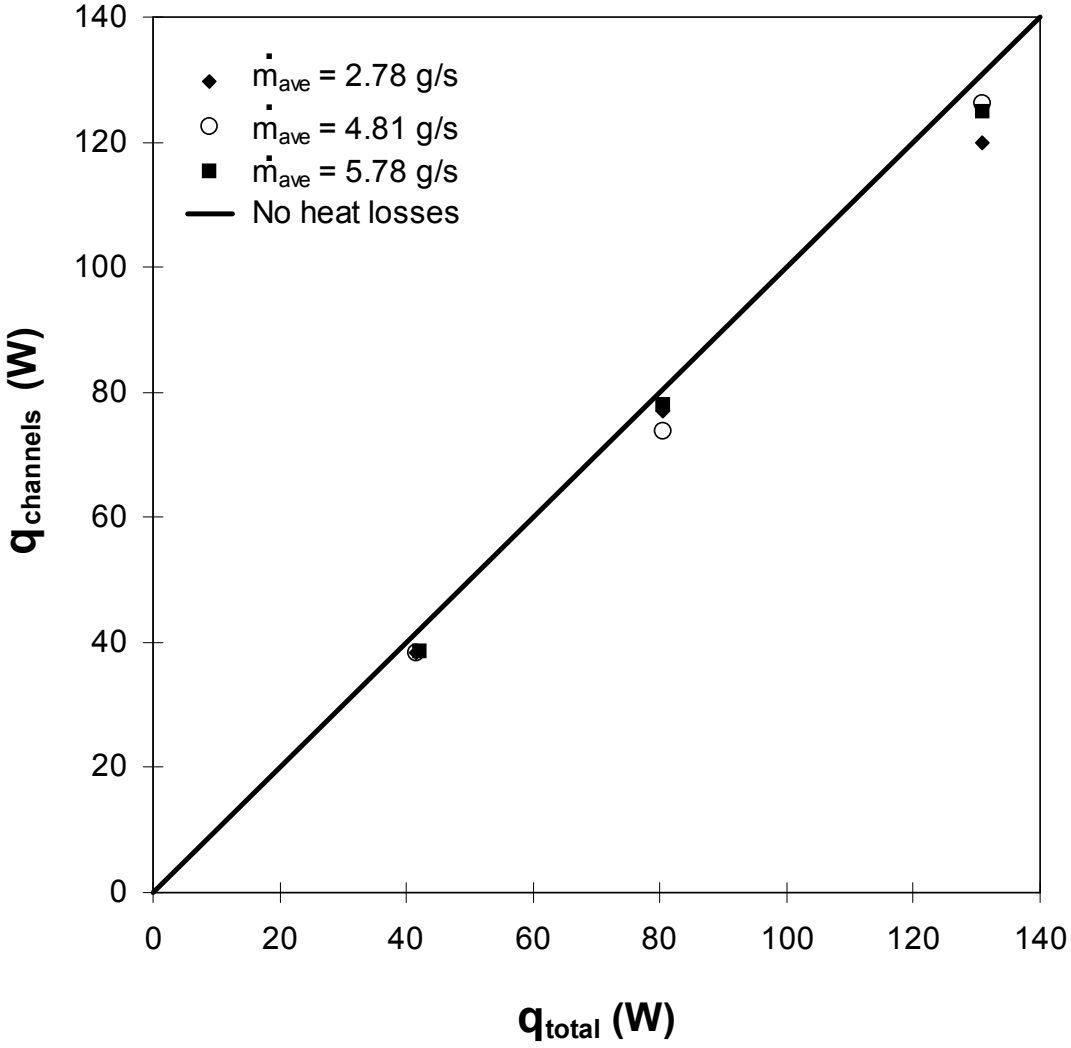

Figure 12. Actual power input into the channels [Equation (15)] versus total power consumed [Equation (13)] for single phase water.

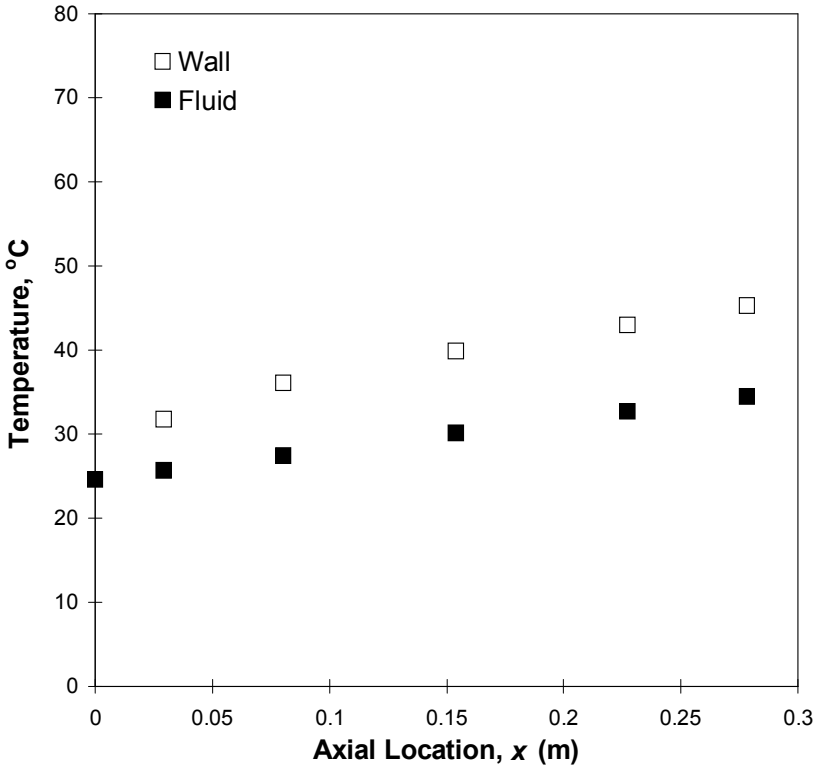

Figure 13a: Fluid and wall temperatures for single phase water at total volumetric flow rate of 2.9×10^{-6} m^3/s and power input of 130 W.

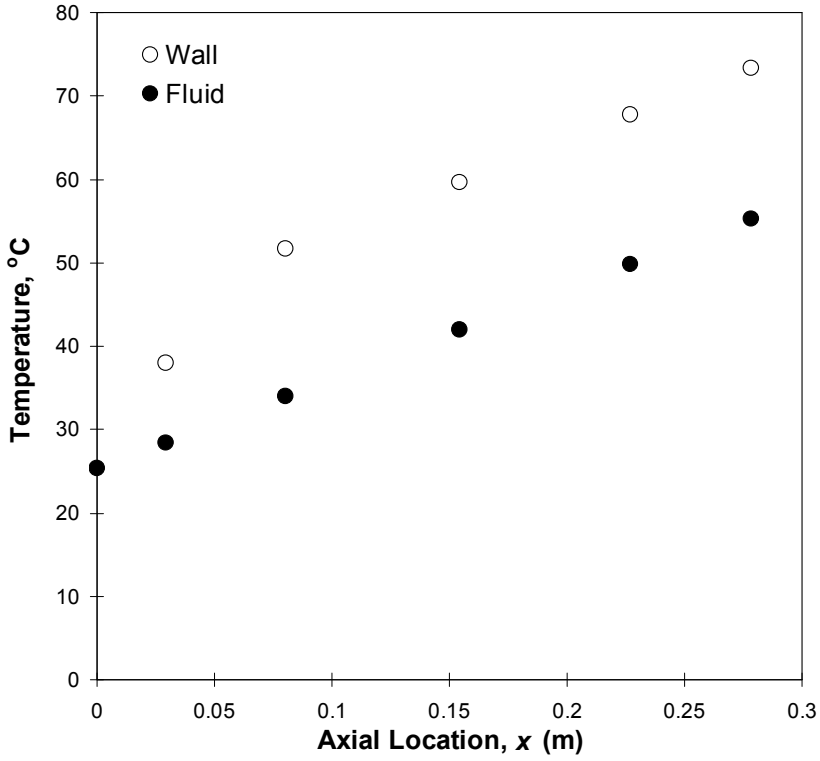

Figure 13b: Fluid and wall temperatures for CGA at total volumetric flow rate of 2.9×10^{-6} m^3/s and power input of 130 W.

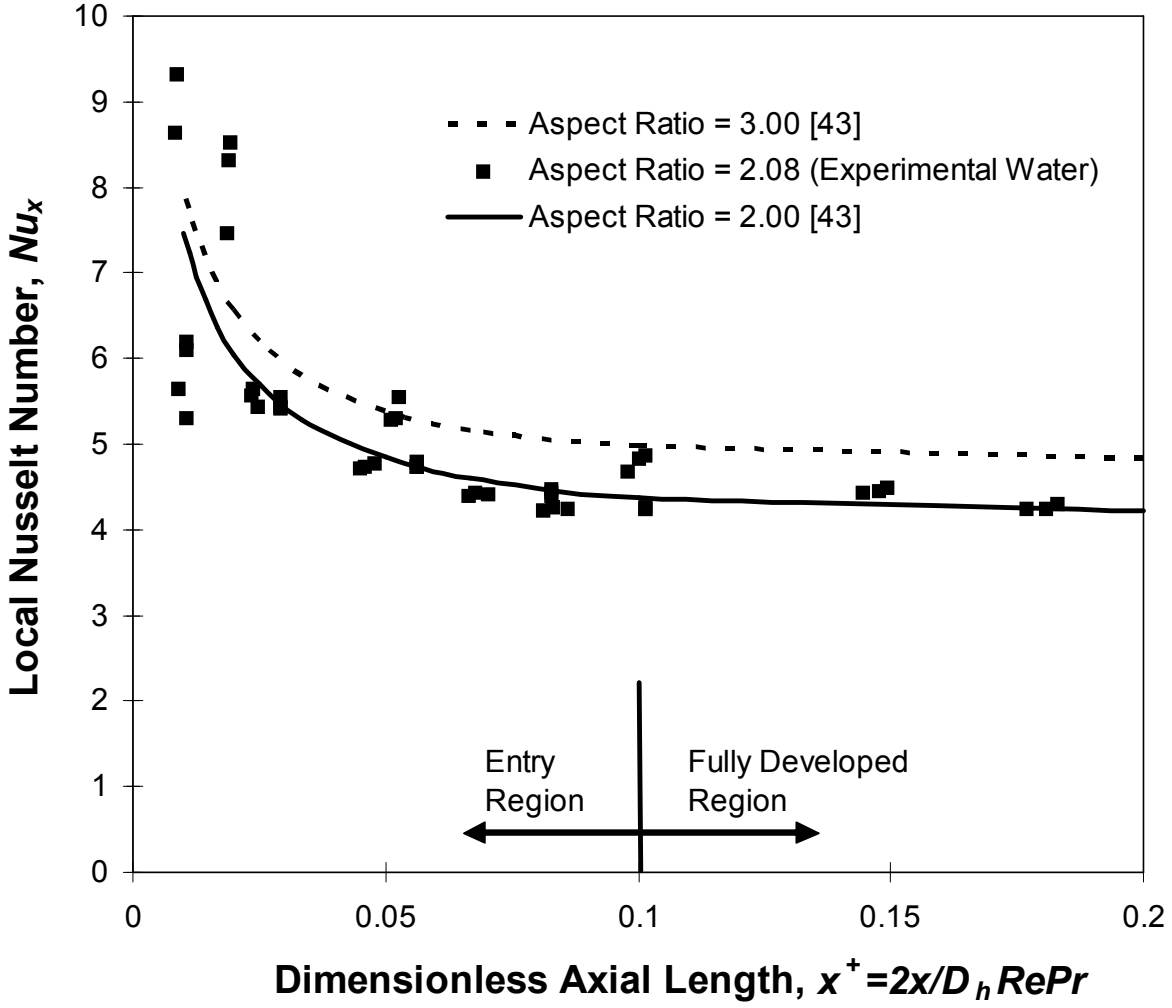

Figure 14. Local Nusselt number along the dimensionless axial length of the channels for single phase water.

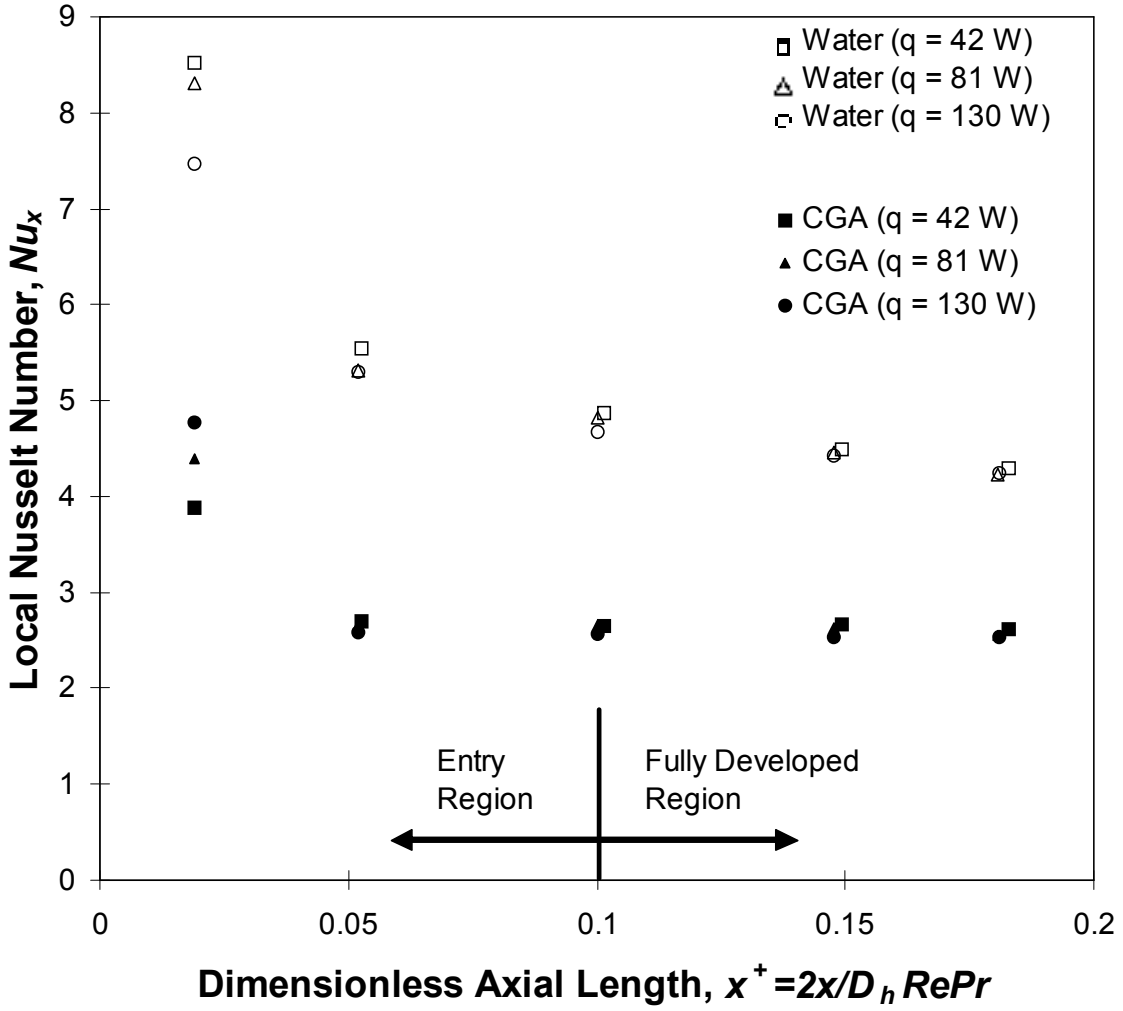

FFigure 15. Comparison of local Nusselt number versus dimensionless axial length for both water and CGA with volumetric flow rates and heat input of 2.68×10^{-6} m^3/s at 42 W, 2.77×10^{-6} m^3/s at 81 W, and 2.90×10^{-6} m^3/s at 130 W.

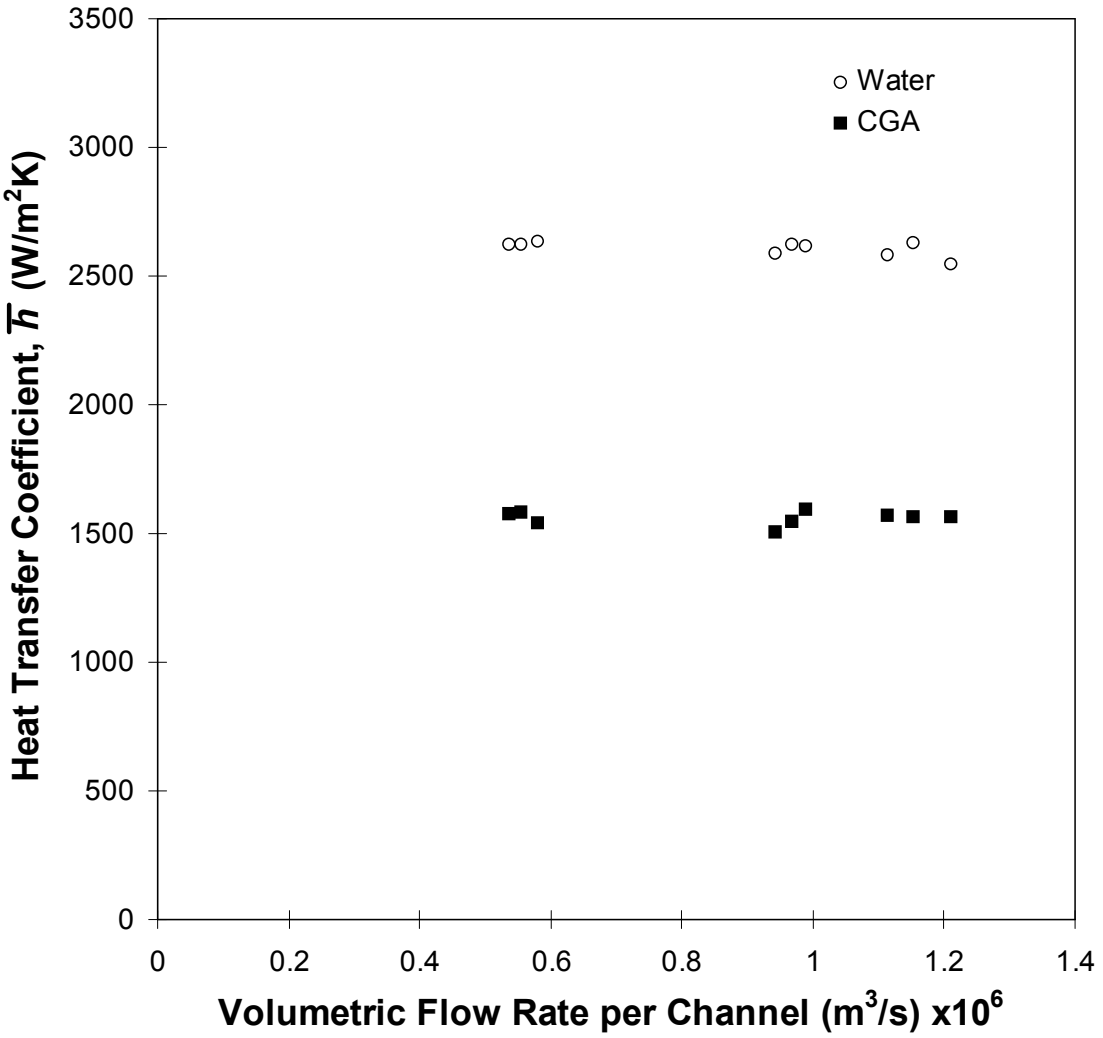

Figure 16. Average heat transfer coefficient in the thermally fully-developed region versus the volumetric flow rate in a single channel for both water and CGA and for different heat fluxes under uniform heat flux.